

Spatially resolved detection of small molecules from press-dried plant tissue using MALDI imaging

Zane G. Long¹  | Jonathan V. Le²  | Benjamin B. Katz¹  | Belen G. Lopez¹  |
 Emily D. Tenenbaum³  | Bonnie Semmling⁴  | Ryan J. Schmidt⁵  |
 Felix Grün¹  | Carter T. Butts⁶  | Rachel W. Martin^{1,2} 

¹Department of Chemistry, University of California, Irvine, California 92697-2025, USA

²Department of Molecular Biology and Biochemistry, University of California, Irvine, California 92697-3900, USA

³Piscataway High School, Piscataway, New Jersey 08854, USA

⁴The Chrysler Herbarium and Mycological Collection, School of Environmental and Biological Sciences, Rutgers University, New Brunswick, New Jersey 08901, USA

⁵Department of Ecology, Evolution, and Natural Resources, Rutgers University, New Brunswick, New Jersey 08901, USA

⁶Departments of Sociology, Statistics, Computer Science, and Electrical Engineering and Computer Science, University of California, Irvine, California 92697, USA

Correspondence

Rachel W. Martin, 1102 Natural Sciences 2, University of California, Irvine, California 92697-2025, USA.
 Email: rwmartin@uci.edu

This article is part of the special issue "Advances in Plant Imaging across Scales."

Abstract

Premise: Matrix-assisted laser desorption/ionization mass spectrometry imaging (MALDI-MSI) is a chemical imaging method that can visualize spatial distributions of particular molecules. Plant tissue imaging has so far mostly used cryosectioning, which can be impractical for the preparation of large-area imaging samples, such as full flower petals. Imaging unsectioned plant tissue presents its own difficulties in extracting metabolites to the surface due to the waxy cuticle.

Methods: We address this by using established delipidation techniques combined with a solvent vapor extraction prior to applying the matrix with many low-concentration sprays.

Results: Using this procedure, we imaged tissue from three different plant species (two flowers and one carnivorous plant leaf). Material factorization analysis of the resulting data reveals a wide range of plant-specific small molecules with varying degrees of localization to specific portions of the tissue samples, while facilitating detection and removal of signal from background sources.

Conclusions: This work demonstrates applicability of MALDI-MSI to press-dried plant samples without freezing or cryosectioning, setting the stage for spatially resolved molecule identification. Increased mass resolution and inclusion of tandem mass spectrometry are necessary next steps to allow more specific and reliable compound identification.

KEYWORDS

chemically specific imaging, in situ chemical analysis, intact plant tissue imaging, MALDI-MSI, mass spectrometry, metabolites

Resumen

Premisa: Matrix-assisted laser desorption/ionization mass spectrometry imaging (MALDI-MSI) es un método de imagen química que puede visualizar distribuciones espaciales de moléculas particulares. Hasta ahora, las imágenes de tejido vegetal han utilizado principalmente la criosección, lo cual puede ser poco práctico para la preparación de muestras de imágenes con áreas grandes, tales como los pétalos completos de una flor. La obtención de imágenes de tejido vegetal no seccionado presenta sus propias dificultades durante la extracción de metabolitos a la superficie, debido a la cutícula cerosa de la planta.

Métodos: Abordamos esto usando técnicas establecidas de deslipidación combinados con una extracción de vapor por solvente antes de aplicar por aspersión la matriz en bajas concentraciones.

Resultados: Usando este procedimiento, obtuvimos imágenes de tejido de tres especies de plantas diferentes (dos flores y una hoja de planta carnívora). Análisis de factorización material de los datos obtenidos revelaron una amplia gama de pequeñas moléculas específicas en plantas con diversos grados de localización en porciones específicas de las muestras de tejido, al igual que facilitó la detección y remoción de las señales de fondo.

Conclusión: Nuestro trabajo demuestra la aplicabilidad de MALDI-MSI hacia muestras de plantas secadas a presión sin congelación o criosección, creando el marco para la identificación de moléculas resueltas espacialmente. Aumento de la resolución de masas e inclusión de la espectrometría de masas en tándem son pasos necesarios para obtener identificación de compuestos más específica y confiable.

In plants, secondary metabolites have numerous functions, including attracting pollinators (Tanaka et al., 2008; Roy et al., 2022), and in carnivorous plants, prey (Hatcher et al., 2020). They block excess ultraviolet radiation (Ferreira et al., 2012), mediate responses to abiotic stress (Godoy et al., 2021), ward off pathogen infection (Kliebenstein et al., 2005), and provide defense against herbivory (Erb and Reymond, 2019). These small molecules are often medically relevant to humans in the form of drugs, initially isolated from plant tissue and then synthesized and improved in the laboratory (Verpoorte, 1998; Atanasov et al., 2015). Understanding pigmentation patterns in plants on a molecular level is important for both agriculture and wider industrial contexts, where coloration can impact a plant's attractiveness to pollinators, or when breeding ornamental plants for unique, commercially valuable coloration patterns. Performing a census of a given plant's repertoire of small molecules provides an overview of the scope of secondary metabolite production for a given species, as well as within-species variation and responses to differing environmental conditions (Moore et al., 2014; Speed et al., 2015; Kessler and Kalske, 2018). Mapping spatial distributions of small molecules in response to plant predation can also provide information about plant defense mechanisms, and could be used to discover novel plant-based pesticides. Identifying the specific parts of plants that produce higher concentrations of small-molecule drugs can guide transcriptomics experiments, enabling the identification of gene clusters responsible for the drug's production (Andersen et al., 2017). This can then pave the way for production in large-scale bioreactors in lieu of less efficient agricultural efforts or traditional synthetic chemistry (Oksman-Caldentey and Inzé, 2004; Marchev and Georgiev, 2020).

Plant metabolites are usually isolated and identified by homogenizing the tissue, extracting fractions in different solvents, followed by chromatographic separation and identification by nuclear magnetic resonance (NMR) spectroscopy and/or mass spectrometry, generally with the assistance of metabolite databases (Wolfender et al., 2019). Although this procedure enables identification of many products from a single specimen, it does not preserve the spatial distribution of chemical species. Retaining this information is highly desirable as a means of both selectively harvesting plant parts that contain the molecule of interest,

and understanding metabolite function in the context of plant biology. Matrix-assisted laser desorption/ionization (MALDI) mass spectrometry imaging (MSI) is a relatively new technique that enables spatial analysis with chemical specificity (Cornett et al., 2007). In MALDI-MSI, a laser is fired at a matrix-coated sample, which is often under vacuum. The matrix is generally a small molecule or mixture thereof that strongly absorbs light at the wavelength of the laser, which then transfers energy to the molecules extracted from the tissue. These analyte molecules are thus desorbed and ionized, followed by detection using a mass spectrometer. Data collection is repeated at many points across the sample, enabling reconstruction of images that map the intensity of a specific ion across the entire region of interest. MALDI-MSI has been used extensively to analyze animal tissues by mapping chemical species ranging from small molecules to proteins, including markers of neurological disease and cancer (Manzo et al., 2020; Gonçalves et al., 2022). Plant tissues have also been analyzed using MALDI-MSI or related techniques such as desorption electrospray ionization (DESI) (Sugahara et al., 2019; Zhang et al., 2021); however, cryosectioning of fresh tissue remains the dominant methodology (Sarabia et al., 2020; Ritmejerjytė et al., 2020, 2022). Methods such as imprinting of tissue into porous materials have also been demonstrated (Muller et al., 2011; Zhang et al., 2021). Targeted analyses of whole plant tissue have showcased the difficulties in sample preparation and matrix application that can limit sensitivity and complicate untargeted data collection (dos Santos et al., 2019). Mapping the spatial distributions of small molecules in whole plant tissues (e.g., entire flower petals and plant leaves) is difficult compared to animal tissues for many reasons. These include the waxy coating present on air-exposed plant organs (Cha et al., 2008) and complications due to metabolite extraction by solvent into the matrix. Although cryosectioning is a valuable technique both for imaging non-surface plant tissues and removing the waxy cuticle, less technically demanding and higher-throughput methods are necessary for the analyses of large-area samples needed to map macro-scale characteristics, such as coloration patterns.

In this work, we demonstrate a general procedure for the facile preparation of press-dried plant tissue samples for analysis by MALDI-MSI. A simple procedure for the drying, delipidation, and application of matrix is outlined, followed

by parameters for data acquisition on the MALDI instrument. We have imaged both flower and leaf tissue from three plant species to highlight the general applicability of the method. *Drosera capensis* L. and *Viola sororia* Willd. are known to contain a variety of polyphenolic compounds (Alston, 1955; Egan and van der Kooy, 2013), including anthocyanins and flavonoids, which may have unique spatial distributions throughout the tissue. *Erigeron glaucus* Ker Gawl. provided conveniently small, individual florets that were used to test different sample preparation conditions. We observed a range of putative non-matrix tissue-specific small molecules in each of the three tissue types, with a range of localization patterns.

METHODS

Study species

Drosera capensis is a carnivorous plant native to the Cape region of South Africa (Slack, 1979). It is characterized by its long leaf blades bearing a multitude of small, elongated glandular trichomes, which secrete a sticky mucilage used to trap prey insects while the leaf blade curls around the prey to further immobilize it. During digestion, the plant releases a wide range of hydrolytic enzymes to break down insect tissue as well as antimicrobial peptides to ward off opportunistic pathogens. The procedure outlined in this paper was initially developed specifically to image *D. capensis* tissues to study these processes, but we found it to be generalizable to other plant tissues.

Viola sororia, or the common blue violet, is native to eastern North America, and is the current state flower of Illinois, Rhode Island, Wisconsin, and New Jersey, where our specimens were collected. Appropriately named, the flower displays a vibrant blue coloration throughout most of the petal. Data from related species suggest that this is due to the production of various anthocyanin pigments (Farzad et al., 2003; Zhang et al., 2012). We plan to use this sample preparation method to map anthocyanin localizations throughout *V. sororia* petals.

Erigeron glaucus, or the seaside daisy, is native to the California coastline. It produces a number of flower heads, each containing a large number of florets, which can range widely in color and intensity. These florets provide a convenient model for assaying different sample preparation conditions, as they are small enough to reasonably allow relatively high-resolution images of multiple whole florets to be captured in a single imaging experiment.

Collection of plant tissue for drying

Erigeron glaucus flower heads were obtained from live plant specimens in cultivation at the University of California, Irvine (UC Irvine), in May 2022. Ray florets were carefully isolated from all other tissue components. Briefly, flower

heads were cut from the plant using clean metal dissecting scissors, including approximately two inches of peduncle. Within 30 min of collection, the florets were gently washed in a deionized water bath containing ice to remove any water-soluble contaminants, and gently patted dry using Kimwipes (Fisher Scientific, Pittsburgh, Pennsylvania, USA). The ray florets were then collected by gently crushing the receptacle of the flower heads with scissors, which loosened the petals and other filamentous portions of the flower head enough to easily isolate the florets without visible damage. The pappus bristles of the ray florets were removed from the base of the corolla using forceps. The top face of the florets (i.e., those facing upward when on the flower head) can be identified by the presence of the stigma. These samples were then used to prepare dried samples.

Drosera capensis leaves were collected from plants grown in cultivation at UC Irvine. Leaf blades were cut to include a few millimeters of petiole. The collected leaf blades were wiped with Kimwipes to remove mucilage, rinsed gently with deionized water, and patted dry with Kimwipes. These sections were then used to prepare dried samples.

Viola sororia specimens were collected in Piscataway, New Jersey. For each population of *V. sororia* sampled, a herbarium voucher was deposited in the Chrysler Herbarium at Rutgers University (CHRB; see Appendix 1 for herbarium voucher information, and the specimen images in the supplemental file folder ‘*Viola sororia* Herbarium Voucher Images’ [available via the Open Science Foundation, see Data Availability Statement]). Flower specimens were packaged in plastic bags containing dry paper towels and shipped to UC Irvine. On arrival, the flower petals were isolated from the rest of the plant tissue and divided into two groups. Both groups were used to prepare drying assemblies, as detailed below. The first group was flash-frozen in liquid nitrogen before being stored at -80°C prior to lyophilization, which resulted in significant visible damage to the flower petals. The second group was dried under ambient conditions, as noted below.

Preparation of plant tissue samples

All collected plant tissue sections (flower petals and leaf blades) were sandwiched between Kimwipes and glass microscopy slides (VWR, Radnor, Pennsylvania, USA), and rubber bands (“Pale Crepe Gold”; Alliance Rubber Company, Hot Springs, Arizona, USA) were used to hold the slides in place. The assemblies were placed in a closed drawer at ambient temperature until use, at least three days after initial assembly. Tissue sections were individually delipidated by immersion in hexanes with gentle inversion for 5 min.

The tissue sections were dried on a Kimwipe and left to air dry for at least 30 s, and the delipidated tissue sections were then affixed to clean, stainless steel slides. Polished stainless steel (316L) MALDI slides (1 in \times 3 in \times 1 mm) were milled by the UC Irvine School of Physical Sciences Machine Shop. TX609 TechniCloth (Texwipe, Kernersville, North Carolina,

USA) was soaked with solvent and placed inside the Petri dish during solvent extraction. Glitter sparkles obtained from Rubber Stampede (Berkeley, California, USA) were used as reference points on the MALDI sample slides. Samples were affixed to the slides using double-sided acrylic tape ("Premium Double Sided Adhesive 1 in × 164 ft", model #4336847256; AJ Sign World, Burnt Hills, New York, USA), trying to maintain a similar orientation for all samples on a slide.

The samples were then pressed into the tape to ensure flatness using a gloved finger over the clean backing. Pre-extraction was then carried out in an 80°C oven, inside a two-part glass Petri dish, with the lower smaller portion containing a circle of thin, absorbent TechniCloth fabric cut to fit inside the dish. The slide was taped to the inside of the upper portion of the Petri dish (avoiding the tape/sample section) with lab tape. Both parts of the Petri dish assembly were pre-heated in the oven for 3 min. Extraction solvent (1 mL, 48.75% methanol/48.75% H₂O/2.5% glacial acetic acid [v/v]) was added to the absorbent pad on the bottom portion of the dish, and the top portion was placed on top, creating a "closed" vapor chamber. HPLC-grade hexanes and methanol were purchased from Fisher Scientific (Pittsburgh, Pennsylvania, USA). The extraction assembly was incubated in the oven for 2 min, then removed to a nearby fume hood where the two parts were separated and allowed to cool to ambient temperature. This process was repeated twice, for a total of three consecutive vapor extractions for each slide.

Matrix solution preparation and application

The matrix solution used consisted of 94.6 mg of α -cyano-4-hydroxycinnamic acid (CHCA; Sigma Aldrich, Burlington, Massachusetts, USA) in 50 mL of 90% methanol/9.9% H₂O/0.1% trifluoroacetic acid (TFA; Amresco, Cleveland, Ohio, USA) (v/v), resulting in 10 mM CHCA in the matrix solvent. Matrix was applied to the sample inside a fume hood via an analytical nebulizer in 30 passes at a distance of 8–10 in, with each pass over the slide lasting approximately 2 s, with a 15-s drying time between passes to avoid solvent buildup. After matrix application, the slide was allowed to dry under a house vacuum inside a vacuum desiccation chamber containing Drierite (W.A. Hammond Drierite Co., Xenia, Ohio, USA). Each sample was dried for at least 1 h, but usually overnight, in order to remove residual solvent before being placed into a MTP Slide Adapter II (Bruker, Billerica, Massachusetts, USA). An optical image of the specimen in the adapter was collected, and then the adapter was placed into the instrument, where it was allowed to pump down to less than 10⁻⁷ mbar before imaging.

Optical images of slide samples

Optical images of slides were captured using an Epson Perfection V600 Photo flatbed scanner (Epson America, Los Alamitos, California, USA). Images were collected using

Professional Mode settings, Reflective document type, Document Table source, and Photo type auto-exposure. Images were captured in 48-bit color at resolutions of 2800–12,800 dpi, depending on the size of the imaged area and the instrumental restriction on image size. The only Adjustment setting enabled was the Unsharp Mask setting, set to High.

Data acquisition

Data were acquired using an UltrafleXtreme MALDI-MSI instrument (Bruker). Positive mode data were acquired with a mass range of 220–1200 Da, using 100 shots per raster spot, at a frequency of 2000 Hz. Instrument settings are noted in Table S1 (available in the supplemental materials via the Open Science Foundation, see Data Availability Statement). Data were acquired at resolutions of 25 μ m (*D. capensis* trichomes), 50 μ m (first of three light and dark *E. glaucus* petals), or 100 μ m (non-trichome *D. capensis* tissue, all *V. sororia* petals, and two other light and dark *E. glaucus* florets). Imaging regions were drawn around the regions of interest, namely the entire petals/florets of *V. sororia* and *E. glaucus*, upper and mid-sections of *D. capensis*, and individual trichome structures of *D. capensis*, using flexImaging software (Bruker). Data for *D. capensis* and *V. sororia* were collected in a single imaging session, across two separately prepared slides, while data for *E. glaucus* were collected in a separate imaging session.

Calibration using cesium iodide (CsI)

The mass analyzer was calibrated using the exact masses of CsI clusters (m/z 392.71534, 652.52253, and 912.33516), spotted/streaked as a 50 mM solution in 90% methanol/9.9% H₂O/0.1% TFA (v/v) on the bare metal of the sample slide to yield small crystals. Spectra were collected to yield sharp, high-intensity peaks for each cluster.

Data processing

Imaging data were processed using SCLS Lab software (version 10.01.13622; Bruker). Data were processed in reduced form (spectra were reduced to 8000 data points across the range of 200–1200 Da, via a flexImaging preference setting). Only sections of the same plant species on the same sample slides were processed together as a group, to ensure comparability and limit artificial signal differences stemming from inter-sample matrix application variability and sensitivity changes of the instrument over time. Additionally, lower- and higher-resolution sections of the same tissue (except for the tape background section) were processed separately to generate ion images due to an apparent difference in signal between the groups.

All data were processed using total ion count (TIC) normalization and a width of 0.5 Da. Images were generated with hot-spot removal enabled, using a Quantile setting of 95%. The interval processing mode was set to use peak area, rather than peak intensity, to account for the wide mass bands.

Once the desired imaging data were selected in flexImaging, regions were manually drawn around the tissue sections in the imaged areas. An additional region was drawn to encompass the section of tape not containing tissue, which served as a background comparison. The average spectrum of the tissue-containing regions was manually compared to the average spectrum of the tape-only background section, and tissue-specific peaks were identified and added to a feature list used to generate ion images, with a width of 0.5 Da centered on the top of the peak. Tissue-specific peaks were identified by visually striking localization to the physical location of the tissue in the reference image, compared to the small tape border around the tissue and the tape-only background region. Care was taken to avoid picking two peaks in the same isotope distribution (within 1–2 Da), unless it was clear based on the different patterns of localization that the two peaks represented distinctly different species (which was rare). This localization was confirmed for each of the identified peaks by comparing the spectra of the tissue-containing regions to the tape-only region via a Kruskal–Wallis test (Kruskal and Wallis, 1953). The large width was used after observation of significant mass shifts (relative to the practical limits of the instrument) due to height variation across the sample (<0.5 Da), which we had observed to be high relative to more typical microtome-sliced samples.

To confirm that the observed ion features corresponded to the physical location of the tissue samples, Kruskal–Wallis tests were performed to compare the intensity distributions of tissue sections between subregions of the same tissue sample, between the individual tissue sections, and between tissue sections and the tape background. The results of these tests are summarized in Tables S2 and S3 (*D. capensis*), Table S4 (*V. sororia*), and Tables S5 and S6 (*E. glaucus*) (see Data Availability Statement). The color images of the imaged tissue sections outlining the regions used for the calculations in Tables S2–S6 are available in Figures S1–S5. The original, unedited images used in the figures for each tissue set, directly exported from the SCiLS Lab software, are available in the supplemental materials (Figures S6–S30; see Data Availability Statement). The original data files, SCiLS Lab files, and additional data and images are available as an included folder.

Material factorization analysis

The processed MALDI-MSI images for each plant sample yield a large voxel by m/z matrix indicating the mix of molecular masses observed at each location. In practice,

however, these patterns are not unique: sampled plant tissue at any given location is composed of a mixture of different compounds, many of which are co-localized. We describe each characteristic set of chemical compounds as a biological material. We can thus greatly simplify analysis by reducing the mass distribution in each voxel to a distribution over a much smaller number of materials, each of which may provide insights into the sample. For instance, one immediate application of such a data factorization is to separate the background signals arising from, for example, the material on which the sample is mounted or the matrix solution from plant-specific signals, thereby allowing them to be removed from subsequent analysis. Materials may also be associated with specific tissues or anatomical features, providing a parsimonious link between chemical composition and plant morphology.

Our analysis proceeds as follows. We assume a set of V voxels, with measurements on M mass (m/z) categories expressed via a $V \times M$ matrix F ; as absolute molecular yields cannot be reliably determined with this method, we take each row of F to be normalized (i.e., to express relative proportions). We approximate each row of F as a weighted combination of d material composition vectors, each of which is a normalized, nonnegative vector of length M representing the distribution of molecular masses comprising its respective material type. Let C be the $M \times d$ matrix of material composition vectors, and let W be the $V \times d$ matrix of voxel composition weights. We then seek a factorization of the form

$$F \approx WC^T, \quad (1)$$

with W being row-normalized, C being column-normalized, F being row-normalized, and all matrices being non-negative. This is a type of normalized non-negative matrix factorization (NMF) problem (Gillis, 2020), and is closely related to (although distinct from) techniques such as singular value decomposition (SVD) (Banerjee and Roy, 2014) and latent Dirichlet allocation (Blei et al., 2003).

The large matrices produced by MALDI-MSI (in our case, 15,620, 24,826, or 40,567 voxels for *D. capensis*, *E. glaucus*, or *V. sororia*, respectively, with $M = 8000$ m/z levels) make the decomposition of Eq. 1 computationally challenging. Although we are not aware of existing algorithms for this problem that satisfy the specific normalization constraints required here, we adapt the well-known NMF algorithm (Lee and Seung, 2001) to the present case by adding a renormalization step in each phase of the C and W calculation, ensuring that the solution always retains dual normalization. We use the generalized Kullback–Liebler (KL) objective function, iterating the algorithm until no element of W or C changes by more than 10^{-4} in absolute value (otherwise terminating at 2000 iterations). The factorization solution was initialized with the non-negative double SVD seeding algorithm (Boutsidis and Gallopoulos, 2008); we use their recommended “average/randomized” variant of the

algorithm. All analyses were implemented using the R statistical computing system (R Core Team, 2022) with C++ extensions using the Rcpp library (Eddelbuettel and François, 2011) and the RSpecra library for scalable SVD (Qiu and Mei, 2022).

The above analysis requires specification of the number of materials, d , to extract; as with other factorization methods, increasing d provides a better approximation to F , at the cost of reduced parsimony. Here, we choose the number of materials for each sample by plotting the marginal reduction in KL divergence for adding a new material, as a function of the number of materials already extracted; this is computed for $d \in 1, \dots, 25$. For all our three cases, extracting more than 10 materials yielded little additional improvement in fit, and we hence take $d = 10$. Visualizations of ΔKL vs. d are shown in Figure S45. The final voxel (W) and material (C) compositions are visualized in Figure 1 and in the supplemental materials (Figures S31–S44; see Data Availability Statement); visualizations were performed using R, along with the viridis (Garnier et al., 2021) and vioplot (Adler and Kelly, 2020) libraries.

RESULTS

We demonstrate our sample preparation and data analysis methods on three plant species: *D. capensis*, *V. sororia*, and *E. glaucus*. Representative images illustrating some of the different distributions of molecules that correspond to anatomical features are presented in Figures 2–6, with other molecular masses observed from the same samples shown in the supplemental materials (see Data Availability Statement). MALDI imaging produces a large amount of data, and the analysis is greatly simplified by considering the biological materials as defined by the observed characteristic groups of chemical compounds rather than the distribution of individual compounds. Throughout, we use “material i ” to refer to the i -th material inferred by the factorization analysis. High-intensity points were identified across the samples containing the molecular masses identified as plant-specific, and these were calibrated post-acquisition to the molecular mass corresponding to the potassium adduct of the matrix. These calibrated molecular masses were then searched against a list of anthocyanin molecular masses sourced from the LipidMaps database (available as LipidMaps Anthocyanins in the supplemental file folder ‘LipidMaps Search’; see Data Availability Statement). The molecular masses were matched as either M+H or M+K adducts across the sampled molecular mass range (available as LipidMaps Hits in the supplemental file folder ‘LipidMaps Search’, see Data Availability Statement), with matching protonated and potassiated adduct pairs being observed for multiple molecules. In summary, 13, 23, and 17 of the identified plant-specific *V. sororia*, *D. capensis*, and *E. glaucus* molecular masses were matched to compounds in this list of anthocyanins.

Drosera capensis

For the tissue sections of *D. capensis* leaves imaged at 100 μm (Figure 2), a total of 45 different molecular masses with specific localization to the plant tissue were observed. This localization was confirmed through Kruskal–Wallis tests (Table S2), comparing the intensity distributions of each molecular mass relative to the tape background, and the differences were all statistically significant ($P < 0.001$). When comparing regions drawn only around the lamina (leaf blade) and only the trichomes attached to the leaf, vs. the tape background, all mass intensity distributions remained significantly different from the tape background. Additionally, when comparing the distributions of the observed masses in the leaf blade to the trichome-only region, all but six of the molecular masses displayed significantly different distributions. We observe a relatively even distribution of molecular masses over the examined range of 220–1200 Da, with the lightest tissue-specific molecular mass of 222.2 ± 0.5 Da and the largest at 979.6 ± 0.5 Da. A few molecular masses (e.g., 228.2, 250.2, and 266.2 ± 0.5 Da) appear relatively evenly distributed over the entirety of the tissue, while other observed species present as more localized, either in the trichomes (e.g., 494.8 and 734.9 ± 0.5 Da) or the leaf blade (336.4 and 593.5 ± 0.5 Da).

For the trichome sections of *D. capensis* imaged at 25 μm , a total of 44 different molecular masses with specific localization to the plant tissue were observed. This localization was confirmed through Kruskal–Wallis tests (Table S3), comparing the intensity distributions of each molecular mass relative to the tape background, and the differences were all statistically significant ($P < 0.001$). We observe a relatively even distribution of molecular masses over the examined range of 220–1200 Da, with the lightest tissue-specific molecular mass at 222.1 ± 0.5 Da and the heaviest at 964.7 ± 0.5 Da. Some molecular masses (e.g., 287.1 ± 0.5 Da) seem to appear throughout the trichome, while others (e.g., 672.0 ± 0.5 Da) appear only in the stalk, and not in the glandular head (Figure 3). The same 228.2 ± 0.5 Da adduct appears in the trichome-only sections, as in the lower-resolution leaf blade regions, with the same even distribution.

Material factorization of the combined 25 and 100 μm data sets revealed four materials out of 10 displayed patterns of localization to the plant tissue. Specifically, material 4 (Figure S31) appears to display a striking localization to the heads of the trichomes 1 and 2; this material (ignoring matrix peaks) is primarily composed of peaks at m/z 271.2, 287.3, 401.2, 417.1, 433.2, 455.2, and 524.2. Material 5 (Figure S32) shows great abundance in the leaf tip and leaf sections; this material (ignoring matrix peaks) is primarily composed of peaks at m/z 234.3, 250.2, 463.7, 533.7, 763.2, and 965.2. Material 9 (Figure S33) appears localized to the trichome stalks and the leaf section; this material (ignoring matrix peaks) is primarily composed of peaks at m/z 234.1, 237.1, 250.1, 271.2, 341.0, 417.1, 445.0, 463.4, 533.5, 650.0,

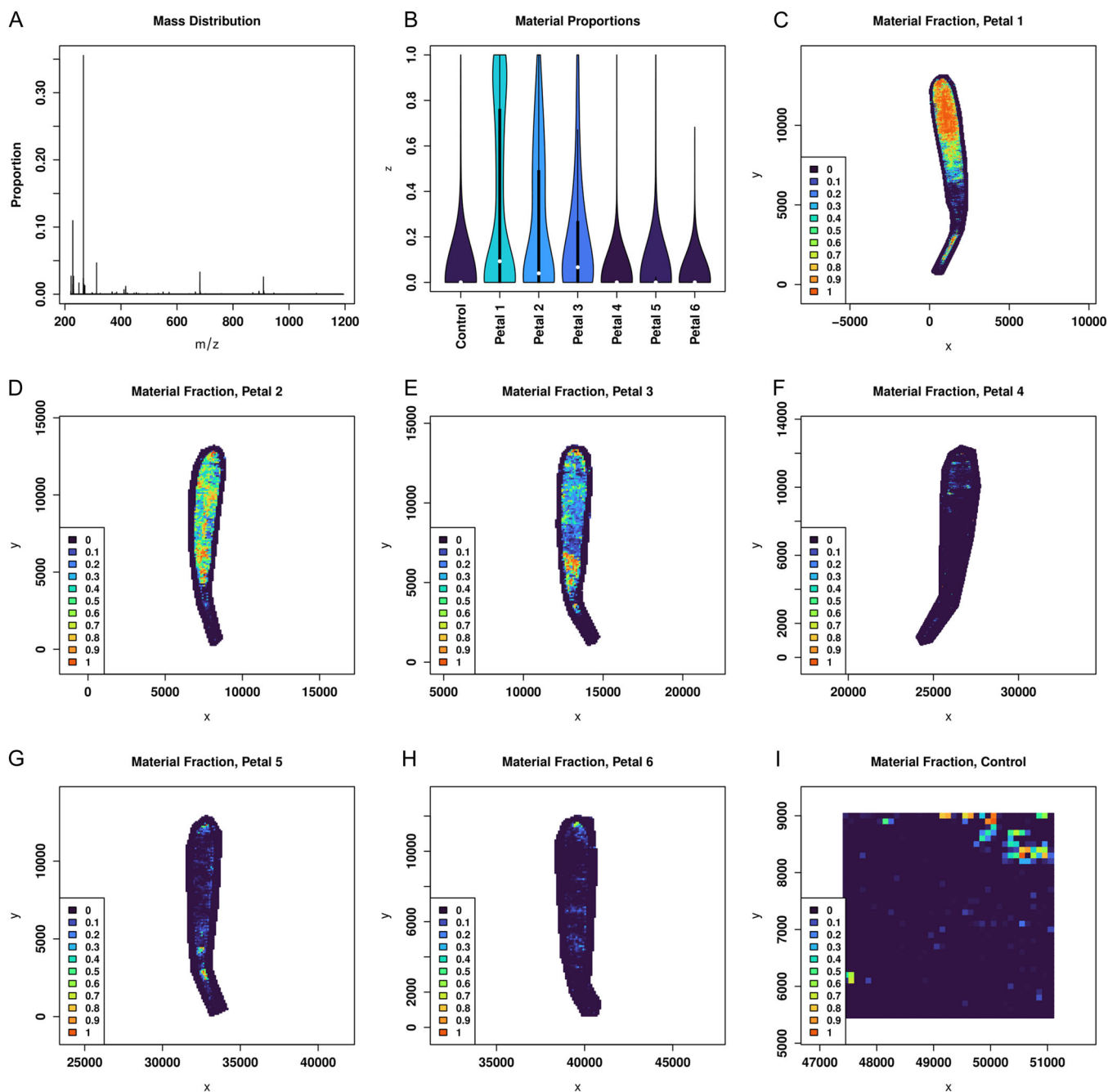


FIGURE 1 Material factorization for *Erigeron glaucus* data, collected at either 50 or 100 μm . (A) This material (2 of 10) is composed of peaks at m/z 230.7, 250.0, 271.0, 313.0, 410.9, 416.9, 681.7, and 908.5. (B) The proportional distributions of material 2 in each voxel of the petals or the control section of the slide. (C–I) Each plot shows the proportion of material 2 in each voxel of the individual petals or the control section of the slide (I). The distribution plot and the images corresponding to each petal indicate that this material makes up a larger proportion of florets 1–3 (the dark florets, C–E), rather than florets 4–6 (the light florets, F–H). Additional material compositions for all three tissue types are available as Figures S31–S44 (see Data Availability Statement).

656.1, 762.8, and 861.0. Material 10 (Figure S34) appears relatively evenly distributed throughout the tissue, with the exception of the center of the leaf tip; this material (ignoring matrix peaks) is primarily composed of peaks at m/z 234.3, 250.2, 379.3, 417.3, 439.2, 463.6, 533.6, 644.1, 650.1, 656.2, 734.9, 762.9, 861.1, and 965.0.

Viola sororia

For the tissue sections of *V. sororia* imaged at 100 μm (Figure 4), a total of 50 different molecular masses with specific localization to the plant tissue were observed. This localization was confirmed through Kruskal–Wallis tests

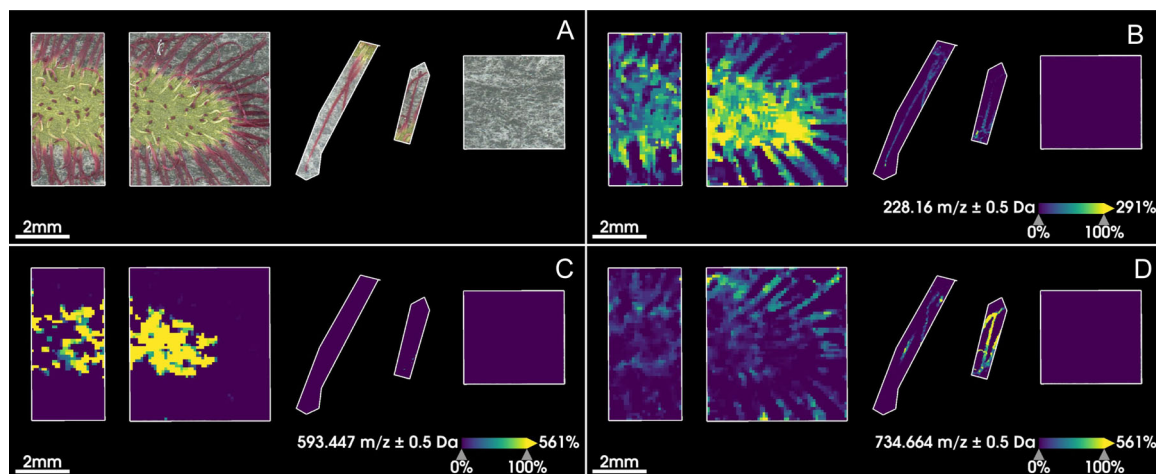


FIGURE 2 MALDI-MSI images for *Drosera capensis* at 100 μm resolution. The subsections in each panel (A–D) correspond to (from left to right) the mid- and upper sections of a *D. capensis* leaf, followed by a tape background section. (A) Optical images of sampled regions. (B) Ion image of the subsections corresponding to $228.2 \text{ m/z} \pm 0.5 \text{ Da}$. The signal appears distributed throughout the leaf, with some concentration in the center of the upper section. (C) Ion image of the subsections corresponding to $593.5 \text{ m/z} \pm 0.5 \text{ Da}$. The signal is localized solely in the non-trichome portions of the leaf, with a spotting pattern, and no signal in the trichomes. (D) Ion image of the subsections corresponding to $734.9 \text{ m/z} \pm 0.5 \text{ Da}$. The signal is localized mainly in the trichomes. Data were collected at 100 μm for both the leaf body and background sections.

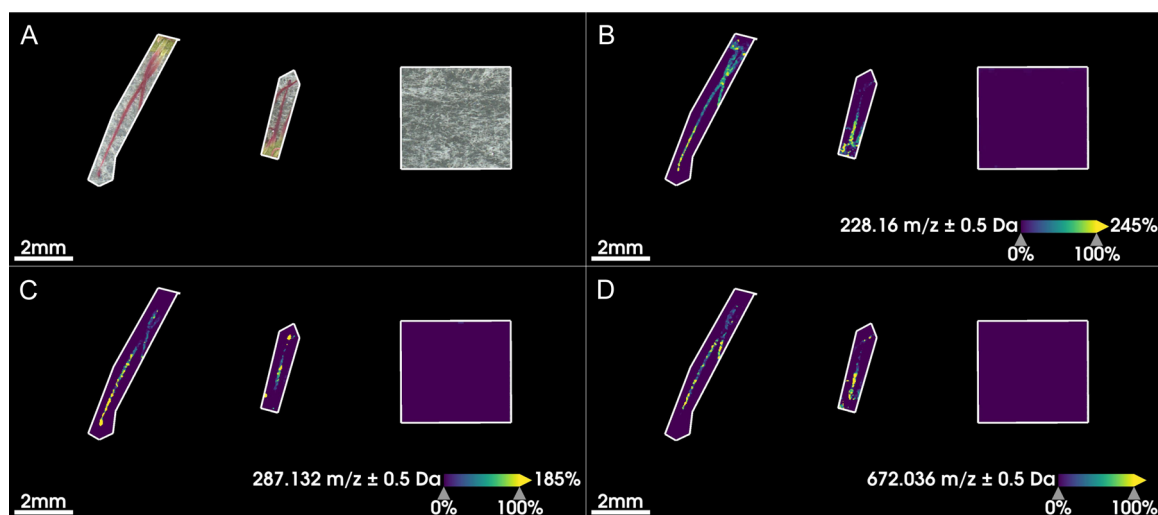


FIGURE 3 MALDI-MSI images for *Drosera capensis* trichomes at 25 μm resolution. The subsections in each panel (A–D) correspond to (from left to right) two detached glandular trichomes from a *D. capensis* leaf, followed by a tape background section. (A) Optical images of sampled regions. (B) Ion image of the subsections corresponding to $228.2 \text{ m/z} \pm 0.5 \text{ Da}$. The signal is present throughout both trichomes, but is more evenly distributed in the first region, with no signal observed in the background section. (C) Ion image of the subsections corresponding to $287.1 \text{ m/z} \pm 0.5 \text{ Da}$. The signal is concentrated in the trichome heads, with a gradient of decreasing abundance in the direction of the leaf blade. (D) Ion image of the subsections corresponding to $672.0 \text{ m/z} \pm 0.5 \text{ Da}$. The signal is concentrated in the stalk of the trichomes. Here, data were collected at 25 μm for the trichome sections and 100 μm for the background section.

(Table S4), comparing the intensity distributions of each molecular mass relative to the tape background, and the differences were all statistically significant ($P < 0.001$). When comparing the groups of press-dried and lyophilized petals to the tape background section by themselves, all distributions remained significantly different from the background. However, there were statistically significant differences between the distributions for 45 out of 50 molecular masses when comparing the press-dried and lyophilized petals to each other. We observe a relatively

even distribution of molecular masses over the examined range of 220–1200 Da, with the lightest tissue-specific molecular mass of $222.0 \pm 0.5 \text{ Da}$ and the heaviest at $1172.1 \pm 0.5 \text{ Da}$. Of the molecular masses observed, many appear relatively evenly distributed over the entirety of the petals (i.e., $266.0 \pm 0.5 \text{ Da}$), while others display greater localization (e.g., $496.4 \pm 0.5 \text{ Da}$ appears localized to the lower left and right side of the petals).

Material factorization of the 100 μm data sets revealed that five materials out of 10 displayed patterns of

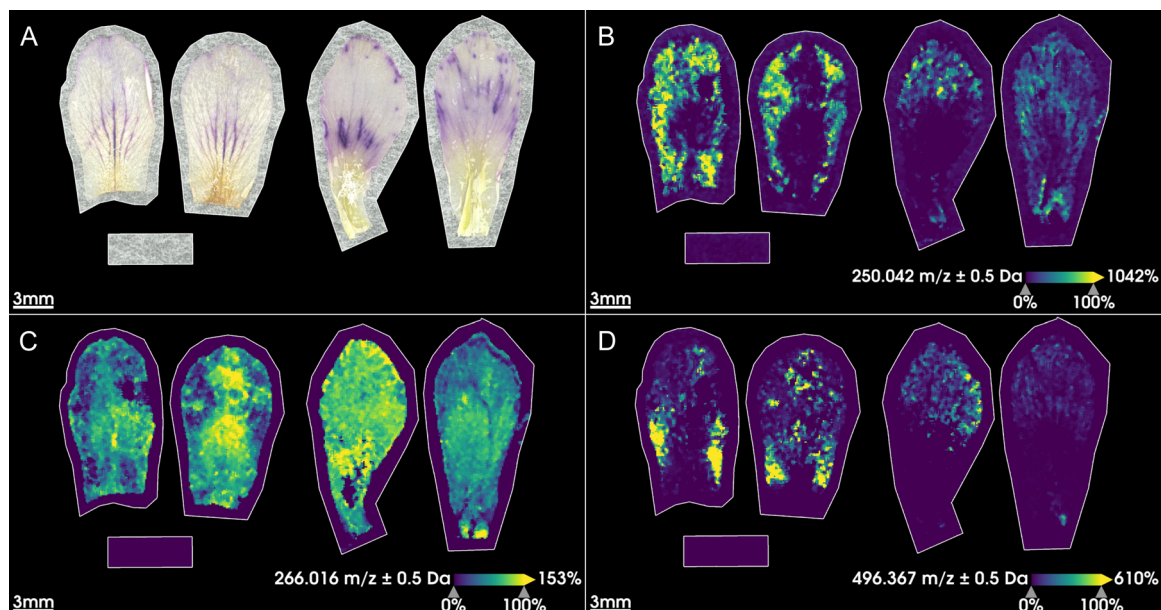


FIGURE 4 MALDI-MSI data for *Viola sororia* at 100 μm resolution. The subsections in each panel (A–D) correspond to (from left to right) two petals that were press-dried and two petals that were lyophilized. A tape background section is shown below the first two petals. (A) Optical images of sampled regions. (B) Ion image of the subsections corresponding to 250.0 $\text{m/z} \pm 0.5$ Da. This signal is more prominent in the press-dried petals, but appears in all petals in all areas except the mid-center of each petal. (C) Ion image of the subsections corresponding to 266.0 $\text{m/z} \pm 0.5$ Da. The signal appears over the entirety of each petal, with moderate localization to the mid-center of each petal. (D) Ion image of the subsections corresponding to 496.4 $\text{m/z} \pm 0.5$ Da. The signal appears mainly in the press-dried petals, localized to the lower left and right side of the two petals. Data were collected at 100 μm for all regions.

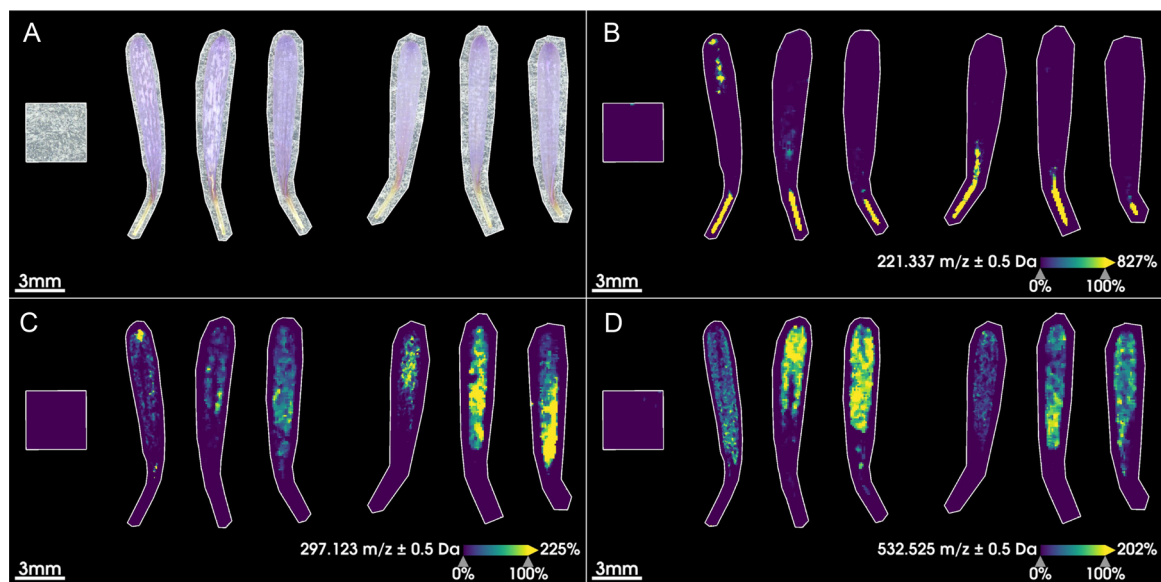


FIGURE 5 MALDI-MSI data for *Erigeron glaucus* imaged at 100 μm . The subsections in each panel (A–D) correspond to (from left to right) two larger, darker florets, two smaller, lighter-colored florets, and a tape background section. (A) Color images of sampled regions. (B) Ion image of the subsections corresponding to 221.3 $\text{m/z} \pm 0.5$ Da. The signal is almost solely localized in the stigmas of the florets, with the exception of the first dark petal, which displays signal near the top of the corolla. (C) Ion image of the subsections corresponding to 297.1 $\text{m/z} \pm 0.5$ Da. The signal appears in both the light and dark petals, but appears more intense in the light florets. (D) Ion image of the subsections corresponding to 532.5 $\text{m/z} \pm 0.5$ Da. The signal appears in both the light and dark florets, but appears more intense in the latter two of three dark florets. Data were collected at 50 μm for the first floret of the dark and light groups, and 100 μm for all other sections.

localization to the plant tissue. Specifically, material 1 (Figure S35) appears to be relatively evenly distributed throughout all the petals, with some seemingly random spotted areas with lower signal; this material (ignoring

matrix peaks) is primarily composed of peaks at m/z 230.7, 236.1, 296.1, 493.0, 682.1, and 909.0. Material 3 (Figure S36) was localized to the lower-to-mid center section of each petal; this material (ignoring matrix peaks) is primarily

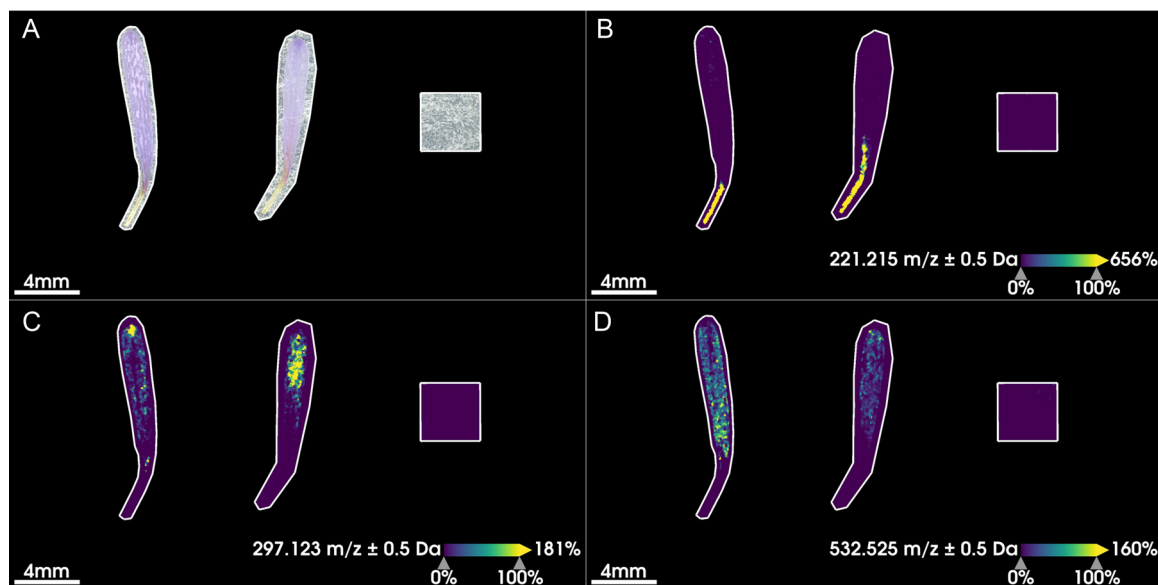


FIGURE 6 MALDI-MSI data for *Erigeron glaucus* imaged at 50 μm . The subsections in each panel (A–D) correspond to (from left to right) a tape background section, three large and dark florets, and three smaller, lighter-colored florets. (A) Color images of imaged subsections of the sample slide. (B) Ion image of the subsections corresponding to 221.2 $\text{m/z} \pm 0.5$ Da. The signal is almost solely localized in the stigmas of the florets, with the exception of the first dark petal, which displays signal near the top of the corolla. (C) Ion image of the subsections corresponding to 297.1 $\text{m/z} \pm 0.5$ Da. The signal appears in both the light and dark petals, but appears more intense in the light florets. (D) Ion image of the subsections corresponding to 532.5 $\text{m/z} \pm 0.5$ Da. The signal appears in both the light and dark florets, but appears more intense in the latter two of three dark florets. Data were collected at 50 μm for the first floret of the dark and light groups, and 100 μm for all other sections.

composed of peaks at m/z 230.7, 250.0, 287.0, 379.1, 492.8, 533.4, 682.0, 894.9, and 909.0. Material 5 (Figure S37) appeared most prominently at the edges of the second lyophilized petal but was also present at low levels in the other three samples; this material (ignoring matrix peaks) is primarily composed of peaks at m/z 230.8, 250.2, 463.6, 533.7, 550.8, 682.2, 909.1, and 965.1. Material 6 (Figure S38) was present in all petals but was most prominent in the two press-dried petals and the second lyophilized petal, at varying levels in each; this material (ignoring matrix peaks) is primarily composed of peaks at m/z 240.2, 250.0, 280.3, 379.1, 455.0, 463.4, 522.6, 533.6, 666.1, 682.1, 893.2, and 965.0. Material 10 (Figure S39) was present at low levels in all petals, observed as small patches of low signal; this material (ignoring matrix peaks) is primarily composed of peaks at m/z 304.4, 332.4, 341.1, 417.4, 457.7, 654.3, 666.4, 729.6, 758.6, 909.5, and 1025.5.

Erigeron glaucus

For the tissue sections of *E. glaucus* imaged at 100 μm (Figure 5), a total of 49 different molecular masses with specific localization to the plant tissue were observed. This localization was confirmed through Kruskal–Wallis tests (Table S5), comparing the intensity distributions of each molecular mass relative to the tape background, and the differences were all statistically significant ($P < 0.001$). When comparing the groups of light and dark florets to the tape background section, all distributions remained significantly

different from background for both groups. However, there were statistically significant differences between the distributions for 35 out of 49 molecular masses when comparing the light and dark florets to each other ($P < 0.05$). We observe a relatively even distribution of molecular masses over the examined range of 220–1200 Da, with the lightest tissue-specific molecular mass of 221.3 ± 0.5 Da and the heaviest at 1184.9 ± 0.5 Da. Of the molecular masses observed, many localize to either the colored corolla (e.g., 532.5 ± 0.5 Da) or the yellowish stigma (e.g., 221.3 ± 0.5 Da). In addition to the same analyses performed on the other tissue types, the imaged regions of each floret were divided roughly into thirds, indicating an “upper,” “midsection,” and “lower” region of each floret. Comparisons of these regions within and across groups (i.e., dark floret upper vs. dark floret lower, dark floret upper vs. light floret upper, etc.) were performed using Kruskal–Wallis tests identically to the previous comparisons (available as ‘*Erigeron glaucus* 100 um.csv’ in the supplemental file folder ‘Kruskal–Wallis Test Results (CSV)’; see Data Availability Statement).

For the tissue sections of *E. glaucus* imaged at 50 μm (Figure 6), a total of 43 different molecular masses with specific localization to the plant tissue were observed. This localization was confirmed through Kruskal–Wallis tests (Table S6), comparing the intensity distributions of each molecular mass relative to the tape background, and the differences were all statistically significant ($P < 0.001$). When comparing the groups of light and dark florets to the tape background section by themselves, all distributions remained significantly different from the background for

both groups, except for one molecular mass for each group (368.4 ± 0.5 Da for the light floret, and 273.2 ± 0.5 Da for the dark floret). However, there were statistically significant differences between the distributions for 38 out of 43 molecular masses when comparing the light and dark florets to each other ($P < 0.05$). We observe a relatively even distribution of molecular masses over the examined range of 220–1200 Da, with the lightest tissue-specific molecular mass of 221.2 ± 0.5 Da and the heaviest at 1184.8 ± 0.5 Da. Of the molecular masses observed, many appear to localize to either the colored corolla (e.g., 532.5 ± 0.5 Da) or the yellowish stigma (e.g., 221.2 ± 0.5 Da). As for the tissue imaged at 100 μm , Kruskal–Wallis comparisons between subregions of the light and dark florets for this set imaged at 50 μm are provided in ‘Erigeron glaucus 50 um.csv’ (available in the supplemental file folder ‘Kruskal-Wallis Test Results (CSV)’; see Data Availability Statement). Material factorization of the data set revealed five materials out of 10 displayed patterns of localization to the plant tissue (Figure 1). Material 1 (Figure S40) displays a relatively even distribution throughout all the florets; this material (ignoring matrix peaks) is primarily composed of peaks at m/z 230.8, 250.1, 313.1, 411.1, 417.1, 681.9, and 908.9. Material 2 (Figure 1, Figure S41) appears entirely localized to the three dark florets; this material (ignoring matrix peaks) is primarily composed of peaks at m/z 230.7, 250.0, 271.0, 313.0, 410.9, 416.9, 681.7, and 908.5. Material 3 (Figure S42) appears entirely localized to the three light florets; this material (ignoring matrix peaks) is primarily composed of peaks at m/z 230.8, 250.2, 271.2, 313.2, 411.2, 417.3, 682.0, and 909.0. Material 6 (Figure S43) presents with low overall abundance but appears in a few small spots in the first and third light florets; this material (ignoring matrix peaks) is primarily composed of peaks at m/z 231.0, 250.3, 271.3, 313.3, 411.3, 682.3, 893.3, and 909.3. Material 10 (Figure S44) appears relatively evenly distributed throughout all the florets but seems to avoid the lower section of each; this material (ignoring matrix peaks) is primarily composed of peaks at m/z 250.1, 271.1, 297.1, 665.9, 681.9, 892.8, 908.8, and 946.1.

DISCUSSION

Practical considerations for sample preparation in MALDI-MSI

Careful attention to sample preparation is critical for obtaining good results with press-dried samples. Here we discuss some practical aspects of specimen handling and matrix application. MALDI-MSI requires electrical contact between the sample and the slide. In this work, multiple conductive tapes were tested, but the best results were obtained with double-sided acrylic tape from AJ Sign World. Although this tape is not advertised as being conductive, it performed the best in our experiments and is inexpensive and easily available.

Many MALDI time-of-flight (MALDI-TOF) instruments, including the Bruker ultrafleXtreme used in this work, place the matrix-coated samples under a high vacuum during analysis and therefore require that samples be pre-dried in order to reach the appropriate vacuum threshold. Samples must also be dry prior to matrix application to prevent the possibility of the drying process significantly disrupting an otherwise even matrix coating, thereby degrading spatial resolution. Many instruments of this type also require samples to be as flat as possible in order to avoid artificial shifts in observed molecular mass values. Such artifacts arise due to the change in path length between the sample (at the spot where the laser fires) and the detector, where even small changes in path length affect the measured time of flight, which is used to calculate the m/z ratio. These shifts correspond to changes in the distance molecules are flying when the same molecule is observed across the sample. In most cases, uneven sample height results in broadening of the m/z peaks. In extreme cases, a relatively large and sudden height difference across the sample can result in one molecule being observed as two or more distinct peaks in the average spectrum. It is quite noticeable when this occurs, as the matrix background signals also suffer from this same mass shift. Our samples are flat enough such that only minor broadening is observed; however, this “minor” broadening is enough that our m/z windows are 0.5 Da, much larger than those ideally allowed by the instrument. The main disadvantage in this is that it prevents two molecules close in mass from being distinguished at the whole-image level, although this problem could be mitigated by using an instrument with secondary fragmentation (MALDI-TOF-TOF). In the absence of such an instrument, the problem is theoretically solvable by the introduction of a calibrant to the matrix solution, followed by post-acquisition correction of mass spectra, which we will explore in future work.

The relative flatness and pre-dried nature of herbarium samples, along with their great abundance and inclusion of old and rare plant species, makes them an interesting target for spatial chemical analysis through MALDI-MSI. The main concerns are flatness on the size scale relevant to time-of-flight measurements and metabolite degradation in the time between sample collection, preparation, storage, and analysis of the dried samples. Heating, which is often used during drying of herbarium samples, may cause accelerated metabolite degradation; therefore, it was not used in this initial study. Differences in metabolite populations due to oxidation or other chemical modification upon heating would be a fruitful direction for future research.

The vouchers for *Viola sororia*, prepared at the Chrysler Herbarium by Ryan J. Schmidt (co-author), were prepared without heating during the drying process. For both the vouchers and larger-scale preparations, corrugated cardboard was used on the opposite side of the blotting paper in contact with the samples in order to increase ventilation. The same procedure was used for smaller samples (i.e., *D. capensis* and *E. glaucus*), except that glass slides were used instead of cardboard. The fresh plant tissue was placed

between layers of Kimwipes, which served as blotting paper. These were then pressed between glass slides, which provide a rigid surface to mold the blotting paper to the samples and maintain flatness. Although the glass is impermeable to moisture and thus could limit airflow, the small size and the total thickness of the paper layers nonetheless enabled rapid drying. We found that the samples were well-dried after two to three days and maintained normal levels of coloration after weeks to months of storage in ambient conditions inside a closed drawer. This small-scale drying preparation was used for small organs such as individual flowers or florets and made it easier to ensure that no tissues overlapped each other.

The samples we chose for analysis were based on availability, relatedness to our overall goal of identifying anthocyanins in plant tissue, and in the case of *D. capensis*, the availability of a draft genome (Butts et al., 2016). We chose a selection of tissues that are known to produce a variety of anthocyanins, and that are relatively thin. Very thick tissue (e.g., from succulents) would present some challenges, both due to flatness and to requirements of the MALDI-MSI instrument. There is a maximum height of the samples allowed above the level of the MALDI slides before the sample touches components inside the instrument. For thick samples, one could theoretically cut slices of the samples prior to drying, such that the dried sample height is less than this maximum; the cut side should then be placed against the tape so that the intact surface is analyzed. Additionally, thicker tissue samples may suffer from lower signal intensity due to lack of conductivity, although we have not yet tested this.

Observed spatial distributions of molecules

From the three tissue types examined in this work, we observed a wide range of molecular masses with varying patterns of localization and species specificity. Because of the limitations imposed on identification due to the mass shifts caused by height variation across each sample, we are unable to definitively identify specific molecules observed here. However, given the m/z range examined (220–1200 m/z) and the use of a standard small molecule matrix (CHCA, $M = 189.04259$ Da), matrix clusters are to be expected, and are likely to present as evenly distributed over the sample. As such, matrix adducts are the most likely explanation of the lower-molecular-weight adducts observed in the samples across species and which present as evenly distributed over the plant tissue. We can putatively identify these molecular masses as matrix clusters: 222.1 ± 0.5 Da ($[\text{CHCA} + \text{MeOH} + \text{H}]^+ = 222.07608$ Da), 228.2 ± 0.5 Da ($[\text{CHCA} + \text{K}]^+ = 228.00575$ Da), and 266.0 ± 0.5 Da ($[\text{CHCA} + 2\text{K} - \text{H}]^+ = 265.96163$ Da). Interestingly, while the potassium adducts are explainable by a higher concentration of potassium in the tissue vs. the tape, the MeOH adduct would presumably be caused by the high methanol concentration in the matrix solvent. However, as this

is sprayed over the entire sample, including the tape, and the samples are placed under vacuum for extended periods before imaging, the pattern of higher signal only in the tissue sample relative to the tape background would seem to require the tissue retaining MeOH more strongly than the tape, or this molecular mass representing a different adduct entirely.

After filtering out the observable matrix adducts, we then asked whether the range of potential identities for the plant-specific molecular masses we observed could be reasonably narrowed down given our wide window of 0.5 Da. All of the plant species examined, or their close relatives, are known to produce a variety of polyphenols, namely flavonoids and anthocyanins. As CHCA has been reported to promote the fragmentation of these molecules to their aglycone forms, we looked to see if such fragments were present in our data set, and observed molecular masses within the appropriate range. The molecular masses of 271.2, 287.1, and 303.1 ± 0.5 Da may correspond to the anthocyanidin fragments pelargonidin ($M^+ = 271.06010$ m/z), aurantinidin and cyanidin ($M^+ = 287.05501$ m/z), and delphinidin ($M^+ = 303.04993$ m/z). In addition, quercetin ($[\text{M} + \text{H}]^+ = 303.04993$ Da, $[\text{M} + \text{K}]^+ = 341.00581$ m/z) also matches some of the observed molecular masses, although the protonated adduct molecular mass is not differentiable from that of a delphinidin fragment with our currently low mass resolution. Further tandem mass spectrometry data are required to make definitive identifications; this will be the topic of a future study.

The molecules detectable by MALDI in a given experiment or sample are highly dependent on both the matrix used for sample preparation and the polarity used during data acquisition. In our case, we used CHCA because it resulted in the widest array of high-intensity peaks. Given the untargeted nature of our analysis, this was the most important factor in the choice of matrix. Other matrices, such as diamionaphthalene (DAN) and dihydroxybenzoic acid (DHB) were trialed in the early stages, and later work will incorporate analyses of different matrices and matrix combinations.

Any untargeted metabolomics method will always have a bias toward certain classes of molecules. Liquid chromatography mass spectrometry (LC-MS) is amenable to different classes of compounds than gas chromatography–mass spectrometry (GC-MS), and both present biases dependent on the mode of sample preparation, extraction, and ionization. MALDI is no different, and in our case, we are able to observe the molecules that are most readily ionized using CHCA as a matrix. Although CHCA has been shown repeatedly to be a very reliable general-purpose matrix, it comes with certain liabilities, like the enhanced hydrolysis of anthocyanins. All other things being equal, higher concentrations will result in greater relative signal, but signal intensity is also dependent on the general ionizability of the compound (e.g., the propensity to make $\text{M} + \text{H}$, $\text{M} + \text{K}$, etc. adducts). In general, formation and observation of protonated adducts ($\text{M} + \text{H}$) is also promoted by the addition of acid (TFA being common for MALDI) to the matrix solution, as used here.

Other problems are caused by the composition of the plant tissue itself. The surfaces of air-exposed plant tissues, including leaves and petals, usually bear some sort of waxy lipid coating. This coating serves multiple roles for the plant, but presents an issue when trying to extract small molecules to the surface for MALDI imaging. In practice, failure to remove this coating leads to most of the observed signal being from these surface lipids, and also largely prevents the matrix solvent from extracting small molecules to the surface from deeper in the tissue. Some researchers have circumvented the problem of the waxy surface and gained access to small molecules deeper in plant tissues through traditional cryosectioning using a microtome (Peukert et al., 2012). We chose to use solvent delipidation to facilitate the preparation of full unsectioned tissue samples, while also minimizing the technical difficulties of the sample preparation.

In order to address these issues without cryosectioning the tissues, we used a mild means of delipidation via immersion of the samples in organic solvent. Hexanes, a common non-polar solvent, has been used previously for delipidation (Hurst et al., 2008). In addition to washing the tissue samples before drying to remove water-soluble molecules on the surface of the tissue, the hexanes wash should remove lipids and other hydrophobic components on the surface. This allows the matrix solvent to penetrate into the tissue and extract molecules to the surface, rather than just observing surface lipids. This extraction is further enhanced by a solvent vapor-based extraction prior to matrix application, which we observed to result in a drastic enhancement of signals across the entire sampled molecular mass range relative to an unextracted control (data not shown). Finally, these preparative steps combined with the large number of matrix application sprays results in even matrix application and extensive extraction of components to the surface to mix with the matrix. Given the lack of any solvent build-up observed during sample preparation, the lack of any apparent metabolite diffusion from the samples into the tape background (based on overlapping the sample and ion images) even for fine tissue details like trichomes (or vice versa), and the apparent steady build-up of very fine matrix crystals, we do not believe diffusion is an issue on a scale relevant to this work for any step in the sample preparation. Additionally, there are many examples of harsher conditions being used to recrystallize the matrix following spray application, or more importantly, when the matrix is sublimed onto samples, so unusual metabolite degradation from this step is unlikely (Yang and Caprioli, 2011). However, the formation of methyl esters when using methanol as a recrystallization solvent could complicate elucidation of compound identities, so future work will also explore the use of different vapor extraction solvents (Dueñas et al., 2016).

Material factorization was useful for identifying groups of co-localized molecular masses. For example, material 4 of *D. capensis* seems to be most abundant in the glandular heads of the trichomes (Figure S31), with prominent peaks

at m/z 271.2 and 401.2, and smaller peaks at m/z 287.3 and 417.1. The two smaller molecular masses may represent pelargonidin and aurantinidin/cyanidin anthocyanidin fragments, where the +130 Da shift observed for both species (m/z 401.2 \rightarrow 271.2 and 417.1 \rightarrow 287.3) indicates similar conjugation or modification of the parent structures. However, if mass shifts across the sample are not accounted for, the factorization may inadvertently create materials that are effectively differentiated by height rather than distinct chemical signatures. For example, material 2 of *E. glaucus* appears most abundant in the dark florets (petals 1–3) (Figure 1), while material 3 appears most abundant in the light florets (petals 4–6) (Figure S42). Inspecting the two materials more carefully reveals a pattern of nearly identical peaks consistently shifted by approximately 0.2 Da (i.e., m/z 271.0, 313.0, 410.9, ... vs. 271.2, 313.2, 411.2, ...). This is likely an artifact of using the raw, binned data sets, instead of peak-picked data processed after a mass-shift correction across the entire sample area using small molecule calibrants.

The factorization methodology employed here results in solutions that are normalized such that every voxel can be written as a convex mixture of materials, and every material can be written as a convex mixture of molecular masses. Although this is more computationally expensive than the related probabilistic latent semantic analysis (PLSA)-based methods of the SCiLS Lab software, the voxels are fixed and the materials are modeled conditional on the voxel, rather than assigning fixed materials to the voxels. This, in particular, allows us to directly interpret voxel composition in terms of proportions of distinct materials, an important prerequisite.

The goal of this work was to develop a method to analyze press-dried plant samples using MALDI-MSI, without requiring tissue cryosectioning while still maximizing the mass and spatial resolution of the data collected. Cryosectioning, sample imprinting, and other sample preparation techniques, combined with different instrumentation (e.g., DESI), can offer higher mass resolution, access metabolites deeper in thick tissues, and even construct three-dimensional representations of metabolite distributions. However, our method offers the advantages of significantly simplified and relatively rapid sample preparation at no apparent cost to spatial resolution for very large sample areas, without the need for advanced instrumentation or sample preparation techniques or equipment. This technique can be used in conjunction with automated methodology for obtaining color information from photos (Luong et al., 2023), providing a molecular-level map of flower colors. The issues we encountered with molecule identification and mass resolution can be improved by using more advanced instrumentation. Nonetheless, our technique allows for the visualization of metabolites in otherwise abundant or press-dried samples, while requiring only a small section of such samples and retaining mass resolution similar to a standard single quadrupole mass detector (0.5 Da). We recognize the limitations in analyzing particularly labile metabolites, which are likely lost during

the drying process and sample storage; however, it seems a waste to ignore the remaining chemical information stored in these otherwise abundant samples. The obvious coloration remaining in the press-dried samples suggests that at least some mildly labile metabolites (anthocyanins) withstand both the drying and matrix application processes. MALDI-MSI has even been successfully performed on ancient clothing samples to analyze dye molecules (Kramell et al., 2019).

CONCLUSIONS

In this work, we present a protocol to analyze press-dried plant samples through MALDI-MSI to determine the spatial distribution of small molecules throughout the tissue sample, using minimal sample preparation, and specifically without the use of cryosectioning techniques. Future endeavors will focus on correcting the mass shifts and low mass resolution due to height variation across the sample through the introduction of one or more CHCA-compatible internal small molecule calibrants (Edmondson and Russell, 1996). These enhancements, combined with secondary fragmentation, liquid chromatography tandem mass spectrometry (LC-MS/MS), and/or GC-MS, will allow for positive structural identification of the observed metabolites. In addition, application of different matrices (i.e., sinapic acid) should allow visualization of proteins, which is especially interesting for the study of carnivorous plants like *D. capensis*, which secretes digestive proteins to its surface during the digestion of prey insects.

AUTHOR CONTRIBUTIONS

Z.G.L., J.V.L., B.B.K., F.G., and R.W.M. planned and designed the experiments. Z.G.L. and J.V.L. performed the experiments, assisted by B.G.L. and B.B.K. Z.G.L. and J.V.L. performed the SCiLS Lab data analysis, with Z.G.L. preparing the related figures. E.D.T., B.S., and R.J.S. oversaw the collection and handling of the *Viola sororia* samples, in concert with Piscataway High School students. B.B.K. and F.G. provided intellectual contributions and guidance in MALDI methods development. C.T.B. performed the materials factorization analysis for all three tissues. Z.G.L., J.V.L., C.T.B., and R.W.M. all made primary contributions and edits to the final manuscript. All authors approved the final version of the manuscript.

ACKNOWLEDGMENTS

The authors thank the students of E.D.T.'s classes at Piscataway High School for collecting the *Viola sororia* samples native to their state. We also acknowledge Elliott Einstein for assistance with anthocyanin identification and Megan Rocha, Gemma Takahashi, and Nicholas Whitman (all from the University of California, Irvine) for helpful discussion and feedback on the manuscript. This work was supported by a Graduate Proposal from the Undergraduate Research Opportunity Program at University of California, Irvine, to Z.G.L.

and NASA Award No. 80NSSC20K0620 to R.W.M. and C.T.B. J.V.L. was supported by the Beckman Fellowship.

DATA AVAILABILITY STATEMENT

Additional supporting information is available via the Open Science Foundation data repository (<https://osf.io/ga4xn/>; DOI 10.17605/OSF.IO/GA4XN). This includes additional images, a list of instrument settings, results of statistical tests, raw color and ion images exported directly from SCiLS Lab for each of the tissues, and plant tissue-specific material factorization plots for each of the tissues. All raw data, SCiLS Lab files, images, and CSV files for all the experiments, as well as the R script used for the material factorization, are also available.

ORCID

Zane G. Long  <http://orcid.org/0000-0002-3795-5551>
 Jonathan V. Le  <http://orcid.org/0000-0002-5030-4817>
 Benjamin B. Katz  <http://orcid.org/0000-0002-0716-9445>
 Belen G. Lopez  <http://orcid.org/0000-0001-6919-8973>
 Emily D. Tenenbaum  <http://orcid.org/0000-0001-8068-3750>
 Bonnie Semmling  <http://orcid.org/0000-0003-2526-8719>
 Ryan J. Schmidt  <http://orcid.org/0000-0002-4907-2270>
 Felix Grün  <http://orcid.org/0000-0002-1891-7285>
 Carter T. Butts  <http://orcid.org/0000-0002-7911-9834>
 Rachel W. Martin  <http://orcid.org/0000-0001-9996-7411>

REFERENCES

- Adler, D., and S. T. Kelly. 2020. vioplot: violin plot. R package version 0.3.7. Website: <https://github.com/TomKellyGenetics/vioplot> [accessed 13 July 2023].
- Alston, R. E. 1955. A study of anthocyanidins produced in *Impatiens balsamina* under the influence of genes determining color types. Ph.D. dissertation, Indiana University, Bloomington, Indiana, USA.
- Andersen, T. B., K. A. Martinez-Swatson, S. A. Rasmussen, B. A. Boughton, K. Jørgensen, J. Andersen-Ranberg, N. Nyberg, et al. 2017. Localization and in-vivo characterization of *Thapsia garganica* CYP76AE2 indicates a role in thapsigargin biosynthesis. *Plant Physiology* 174(1): 56–72.
- Atanasov, A. G., B. Waltenberger, E.-M. Pferschy-Wenzig, T. Linder, C. Wawrosch, P. Uhrin, V. Temml, et al. 2015. Discovery and resupply of pharmacologically active plant-derived natural products: A review. *Biotechnology Advances* 33(8): 1582–1614.
- Banerjee, S., and A. Roy. 2014. Linear algebra and matrix analysis for statistics. Chapman and Hall/CRC Press, Boca Raton, Florida, USA.
- Blei, D. M., A. Y. Ng, and M. I. Jordan. 2003. Latent Dirichlet allocation. *Journal of Machine Learning Research* 3: 993–1022.
- Boutsidis, C., and E. Gallopoulos. 2008. SVD based initialization: A head start for nonnegative matrix factorization. *Pattern Recognition* 41: 1350–1362.
- Butts, C. T., J. C. Bierma, and R. W. Martin. 2016. Novel proteases from the genome of the carnivorous plant *Drosera capensis*: Structural prediction and comparative analysis. *Proteins: Structure, Function, and Bioinformatics* 84(10): 1517–1533.
- Cha, S., H. Zhang, H. I. Ilarslan, E. S. Wurtele, L. Brachova, B. J. Nikolau, and E. S. Yeung. 2008. Direct profiling and imaging of plant metabolites in intact tissues by using colloidal graphite-assisted laser desorption ionization mass spectrometry. *Plant Journal* 55(2): 348–360.
- Cornett, D. S., M. L. Reyzer, P. Chaurand, and R. M. Caprioli. 2007. MALDI imaging mass spectrometry: Molecular snapshots of biochemical systems. *Nature Methods* 4: 828–833.
- dos Santos, N. A., L. M. de Souza, F. E. Pinto, C. d. J. Macrino, C. M. de Almeida, B. B. Merlo, P. R. Filgueiras, et al. 2019. LDI and

- MALDI-FT-ICR imaging MS in Cannabis leaves: Optimization and study of spatial distribution of cannabinoids. *Analytical Methods* 11(13): 1757–1764.
- Dueñas, M. E., L. Carlucci, and Y. J. Lee. 2016. Matrix recrystallization for MALDI-MS imaging of maize lipids at high spatial resolution. *Journal of the American Society for Mass Spectrometry* 27(9): 1575–1578.
- Eddelbuettel, D., and R. François. 2011. Rcpp: Seamless R and C++ integration. *Journal of Statistical Software* 40(8): 1–18. <https://doi.org/10.18637/jss.v040.i08>
- Edmondson, R. D., and D. H. Russell. 1996. Evaluation of matrix-assisted laser desorption ionization-time-of-flight mass measurement accuracy by using delayed extraction. *Journal of the American Society for Mass Spectrometry* 7(10): 995–1001.
- Egan, P. A., and F. van der Kooy. 2013. Phytochemistry of the carnivorous sundew genus *Drosera* (Droseraceae): Future perspectives and ethno-pharmacological relevance. *Chemistry & Biodiversity* 10(10): 1774–1790.
- Erb, M., and P. Reymond. 2019. Molecular interactions between plants and insect herbivores. *Annual Review of Plant Biology* 70: 527–557.
- Farzad, M., R. Griesbach, J. Hammond, M. R. Weiss, and H. G. Elmendorf. 2003. Differential expression of three key anthocyanin biosynthetic genes in a color-changing flower, *Viola cornuta* cv. Yesterday, today and tomorrow. *Plant Science* 165(6): 1333–1342.
- Ferreira, M. L. F., S. P. Rius, and P. Casati. 2012. Flavonoids: Biosynthesis, biological functions, and biotechnological applications. *Frontiers in Plant Science* 3: 722.
- Garnier, S., N. Ross, R. Rudis, A. P. Camargo, M. Sciaini, and C. Scherer. 2021. viridis: Colorblind-friendly color maps for R. R package version 0.6.2. Website: <https://sjmgarnier.github.io/viridis/> [accessed 13 July 2023].
- Gillis, N. 2020. *Nonnegative matrix factorization*. Society for Industrial and Applied Mathematics, Philadelphia, Pennsylvania, USA. <https://doi.org/10.1137/1.9781611976410>
- Godoy, F., K. Olivos-Hernández, C. Stange, and M. Handford. 2021. Abiotic stress in crop species: Improving tolerance by applying plant metabolites. *Plants* 10(2): 186.
- Gonçalves, J. P. L., C. Bollwein, A. M. Schlitter, M. Kriegsmann, A. Jacob, W. Weichert, and K. Schwamborn. 2022. MALDI-MSI: A powerful approach to understand primary pancreatic ductal adenocarcinoma and metastases. *Molecules* 27(15): 4811.
- Hatcher, C. R., D. B. Ryves, and J. Millett. 2020. The function of secondary metabolites in plant carnivory. *Annals of Botany* 125(3): 399–411.
- Hurst, W. J., J. A. Glinski, K. B. Miller, J. Apgar, M. H. Davey, and D. A. Stuart. 2008. Survey of the trans-resveratrol and trans-piceid content of cocoa-containing and chocolate products. *Journal of Agricultural and Food Chemistry* 56(18): 8374–8378.
- Kessler, A., and A. Kalske. 2018. Plant secondary metabolite diversity and species interactions. *Annual Review of Ecology, Evolution, and Systematics* 49: 115–138.
- Kliebenstein, D. J., H. C. Rowe, and K. J. Denby. 2005. Secondary metabolites influence *Arabidopsis/Botrytis* interactions: Variation in host production and pathogen sensitivity. *Plant Journal* 44(1): 25–36.
- Kramell, A. E., M. García-Altare, M. Pötsch, R. Kluge, A. Rother, G. Hause, C. Hertweck, and R. Csuk. 2019. Mapping natural dyes in archeological textiles by imaging mass spectrometry. *Scientific Reports* 9(1): 2331.
- Kruskal, W. H., and W. A. Wallis. 1953. Errata: Use of ranks in one-criterion variance analysis. *Journal of the American Statistical Association* 48(264): 907–911.
- Lee, D. D., and H. S. Seung. 2001. Algorithms for non-negative matrix factorization. *Advances in Neural Information Processing Systems* 13: 556–562.
- Luong, Y., A. Gasca-Herrera, T. M. Misiewicz, and B. E. Carter. 2023. A pipeline for rapid collection of color data from photographs. *Applications in Plant Sciences* 11(5): e11546.
- Manzo, T., B. M. Prentice, K. G. Anderson, A. Raman, A. Schalck, G. S. Codreanu, C. B. N. Lauson, et al. 2020. Accumulation of long-chain fatty acids in the tumor microenvironment drives dysfunction in intrapancreatic CD8⁺ T cells. *Journal of Experimental Medicine* 217(8): e20191920.
- Marchev, A. S., and Z. P. Y. M. I. Georgiev. 2020. Green (cell) factories for advanced production of plant secondary metabolites. *Critical Reviews in Biotechnology* 4(40): 443–458.
- Moore, B. D., R. L. Andrew, C. Külheim, and W. J. Foley. 2014. Explaining intraspecific diversity in plant secondary metabolites in an ecological context. *New Phytologist* 201(3): 733–750.
- Muller, T., S. Oradu, D. R. Ifa, R. G. Cooks, and B. Krautler. 2011. Direct plant tissue analysis and imprint imaging by desorption electrospray ionization mass spectrometry. *Analytical Chemistry* 83(14): 5754–5761.
- Oksman-Caldentey, K.-M., and D. Inzé. 2004. Plant cell factories in the post-genomic era: New ways to produce designer secondary metabolites. *Trends in Plant Science* 9(9): 433–440.
- Peukert, M., A. Matros, G. Lattanzio, S. Kaspar, J. Abadia, and H.-P. Mock. 2012. Spatially resolved analysis of small molecules by matrix-assisted laser desorption/ionization mass spectrometric imaging (MALDI-MSI). *New Phytologist* 193(3): 806–815.
- Qiu, Y., and J. Mei. 2022. RSpectra: Solvers for large-scale eigenvalue and SVD problems. R package version 0.16-1. Website: <https://CRAN.R-project.org/package=RSpectra> [accessed 13 July 2023].
- R Core Team. 2022. R: A Language and Environment for Statistical Computing. R Foundation for Statistical Computing, Vienna, Austria. Website: <https://www.R-project.org/> [accessed 13 July 2023].
- Ritmejerytė, E., B. A. Boughton, M. J. Bayly, and R. E. Miller. 2020. Unique and highly specific cyanogenic glycoside localization in stigmatic cells and pollen in the genus *Lomatia* (Proteaceae). *Annals of Botany* 126(3): 387–400.
- Ritmejerytė, E., R. E. Miller, M. J. Bayly, and B. A. Boughton. 2022. Visualization of cyanogenic glycosides in floral tissues. In D. J. Beale, K. E. Hillier, A. C. Warden, O. A. H. Jones [eds.], *Applied environmental metabolomics: Community insights and guidance from the field*, 29–44. Elsevier, London, United Kingdom.
- Roy, R., N. Moreno, S. A. Brockman, A. Kostanecki, A. Zambre, C. Holl, E. M. Solhaug, et al. 2022. Convergent evolution of a blood-red nectar pigment in vertebrate-pollinated flowers. *Proceedings of the National Academy of Sciences, USA* 119(5): e2114420119.
- Sarabia, L. D., B. A. Boughton, T. Rupasinghe, D. L. Callahan, C. B. Hill, and U. Roessner. 2020. Comparative spatial lipidomics analysis reveals cellular lipid remodelling in different developmental zones of barley roots in response to salinity. *Plant, Cell & Environment* 43(2): 327–343.
- Slack, A. 1979. *Carnivorous plants*. MIT Press, Cambridge, Massachusetts, USA.
- Speed, M. P., A. Fenton, M. G. Jones, G. D. Ruxton, and M. A. Brockhurst. 2015. Coevolution can explain defensive secondary metabolite diversity in plants. *New Phytologist* 208(4): 1251–1263.
- Sugahara, K., K. Kitao, T. Watanabe, and T. Yamagaki. 2019. Imaging mass spectrometry analysis of flavonoids in blue viola petals and their enclosure effects on violanin during color expression. *Analytical Chemistry* 91(1): 896–902.
- Tanaka, Y., N. Sasaki, and A. Ohmiya. 2008. Biosynthesis of plant pigments: Anthocyanins, betalains and carotenoids. *Plant Journal* 54: 733–749.
- Verpoorte, R. 1998. Exploration of nature's chemodiversity: The role of secondary metabolites as leads in drug development. *Drug Discovery Today* 3(5): 232–238.
- Wolfender, J.-L., J.-M. Nuzillard, J. J. J. van der Hoof, J.-H. Renault, and S. Bertrand. 2019. Accelerating metabolite identification in natural product research: Toward an ideal combination of liquid chromatography-high-resolution tandem mass spectrometry and NMR profiling, in silico databases, and chemometrics. *Analytical Chemistry* 91(1): 704–742.
- Yang, J., and R. M. Caprioli. 2011. Matrix sublimation/recrystallization for imaging proteins by mass spectrometry at high spatial resolution. *Analytical Chemistry* 83(14): 5728–5734.
- Zhang, C., A. Žukauskaitė, I. Petřík, A. Penčík, M. Hönjg, J. Grúz, J. Šíroková, et al. 2021. In situ characterisation of phytohormones from wounded *Arabidopsis* leaves using desorption electrospray ionisation mass spectrometry imaging. *Analyst* 146(8): 2653–2663.
- Zhang, J., L.-S. Wang, J.-M. Gao, Y.-J. Xu, L.-F. Li, and C.-H. Li. 2012. Rapid separation and identification of anthocyanins from flowers

of *Viola yedoensis* and *V. prionantha* by high-performance liquid chromatography–photodiode array detection–electrospray ionisation mass spectrometry. *Phytochemical Analysis* 23(1): 16–22.

How to cite this article: Long, Z. G., J. V. Le, B. B. Katz, B. G. Lopez, E. D. Tenenbaum, B. Semmling, R. J. Schmidt, et al. 2023. Spatially resolved detection of small molecules from press-dried plant tissue using MALDI imaging. *Applications in Plant Sciences* 11(5): e11539.
<https://doi.org/10.1002/aps3.11539>

Appendix 1. Herbarium voucher information for *Viola sororia* samples. All specimens are deposited at the Chrysler Herbarium (CHRB), Rutgers University, New Brunswick, New Jersey, USA. Information presented: Collector names and specimen number, collection date, herbarium voucher ID.

Schmidt, Semmling, & Tenenbaum 1066, 14 April 2022, CHRB0105384; Schmidt, Semmling, Tenenbaum, et al. 1068, 27 April 2022, CHRB0112456; Schmidt, Semmling, Tenenbaum, et al. 1069, 27 April 2022, CHRB0112457; Schmidt, Semmling, Tenenbaum, et al. 1070, 27 April 2022, CHRB0112458.